

FeSe as a Polymorphous Network

Zhi Wang¹, Xingang Zhao¹, Robert Koch², Simon J. L. Billinge^{2,3} and Alex Zunger^{1*}

¹*University of Colorado, Renewable & Sustainable Energy Institute, Boulder, Colorado 80309, USA*

²*Condensed Matter Physics and Materials Science Department, Brookhaven National Laboratory, Upton, NY
11973*

³*Department of Applied Physics and Applied Mathematics, Columbia University, New York, New York 10027, USA*

The observed electronic structure of FeSe has lower apparent symmetry than the one suggested by its macroscopic crystallographic structure. It has been argued that such nematicity must be electronic symmetry lowering, driven by strong correlations, rather than a local structural symmetry lowering, the latter being judged on the observation of a too small global structural symmetry lowering. Standard structure predictions use small unit cells that cannot accommodate structural symmetry lowering. Using a predictive first principles minimization of the internal total energy without restricting the system to a small unit cell reveals that the lowest energy configuration whose average macroscopic symmetry is tetragonal consists of a distribution of different local low-symmetries. This polymorphous network explains the observed Pair Distribution Function (PDF) pattern in both the local and long-range regions without a fit. When used as input to electronic structure calculations, the predicted polymorphous structure reveals electronic symmetry breaking that is unique to this unusual compound.

Understanding the physics behind the tendency of materials to remove the degeneracy of electronic states has occupied a central role in condensed matter physics, ranging from semi-classical (size-effect) symmetry-removing distortions^{1,2}, to Peierls dimerization³, and Jahn-Teller⁴ instabilities. Such degeneracy removing events can be structural or electronic in origin. For example, FeSe in its orthorhombic (and tetragonal) phase manifests nematicity⁵⁻⁹, a state where its observed electronic structure has lower apparent symmetry than suggested by its crystallographic structure observed in X-ray diffraction. On the basis that the symmetry-lowering modification of the electronic states is much larger than expected based on the magnitude of the structural symmetry lowering, it has been argued⁵⁻⁹ that such nematicity must be an *electronic* symmetry lowering, driven by strong correlations. However, recent experimental studies using structural probes sensitive to the *local* structure¹⁰ indicate a local structural symmetry lowering that is much larger than seen in the average structure¹¹⁻¹³. This result is on the surface surprising and unexpected, and demands explanation, because it suggests that the structural phases of these materials is not simply the observed crystal structure as gleaned from X-ray Bragg diffraction. In fact, the crystal structure obtained from X-ray Bragg diffraction yields a *periodically averaged* representation of the structure, describable by minimally sized unit cells. It has long been known that at any instant atoms deviate from their periodically averaged crystallographic positions due to thermal motion¹⁴ or stochastic alloy disorder^{15,16}. However, it is possible that some compounds would manifest interdependent local structural motifs that do not order over long-range¹⁷⁻¹⁹: Such compounds manifesting a distribution of different local environments ('polymorphous networks') as a result of the chemical bonding preferences reflected by the *internal energy*, not entropy. Examples include positional local structural motifs (such as off-site local displacements, rigid body rotations, and bond tilting^{1,20-22} in halide perovskites¹⁹) as well as spin local motifs (in 3d oxide paramagnets^{17,18}) found by minimizing the low-T internal energy and require for their description larger than minimal crystallographic cells. While temperature-induced motions at high T can contribute and enhance such displacements, these important, chemically mandated *intrinsic local configurations* could include various symmetry-breaking modes capable of removing electronic degeneracies such as nematicity.

Here we show that FeSe, a chemically simple exemplar of the iron-based high temperature superconductors, falls into the class of polymorphous networks. This is a new prototype polymorphous structure, different from all other known classes¹⁷⁻¹⁹. We use a single-determinant mean-field density functional theory (DFT) — unable to break electronic symmetry without breaking structural symmetry — to perform structural optimization. To do so we employ large unit cells that, unlike the symmetry-constrained minimal unit cell commonly used in fitting X-Ray diffraction structures and in band theory²³⁻²⁵, can yield a lower local structural symmetry if it is

energetically favorable. We find that such first-principles structural optimization predicts that FeSe has a high global-symmetry (e.g. tetragonal) with low local-symmetry network that leads to degeneracy removal. The ensuing polymorphous network (i) has lower total energy than any monomorphous (single motif) unit cell; (ii) provides excellent agreement (without a fit) with the experimental PDF in both the short-range (local) and the long-range, while all monomorphous approaches^{11–13} result in significant deviations. (iii) Identifies pertinent local geometrical coordinates, such as the position-dependent local orthorhombicity $\eta(r)$, that agree well with advanced structural measurements¹² and indicate an enhanced local structural nematicity; (iv) leads to the removal of orbital degeneracy in the electronic band structure; (v) When the bands of the large polymorphous supercell are unfolded^{26–28}, to obtain an Effective Band Structure (EBS), this results for the paramagnetic order in a band structure that reproduces the angle-resolved photoemission spectroscopy (ARPES) observed Fe 3d bands without the need of electron-electron correlation effects that are commonly invoked to explain the measurements.

Identifying the polymorphous nature

Materials that manifest a distribution of different local structural motifs are well known in stochastic systems, e.g. disordered alloys that are thermally stabilized by entropy^{15,16}. But compounds might also develop non-thermal intrinsic local displacement patterns already at low temperature in pure (non-alloyed) ordered compounds. Such structures are the “adaptive structures”, appearing as low temperature vacancies ordering in ScS²⁹, or the large unit cell ground state structures of ordered AuPd³⁰. More recently, such ‘*Polymorphous networks*’ have been taken to explain experimental observations of local symmetry breaking in systems that are not, on the surface, stochastic in nature such as cubic halide perovskites¹⁹. Polymorphous networks are distinguished from the standard monomorphous cases described by a single (or very few) repeated local motif such as the celebrated tetrahedron in covalent semiconductors or the octahedron in perovskites. The existence of local structural displacements in polymorphous networks can have a significant effect on calculated band structure and spectroscopic features if the characteristic length scale of wavefunction compactness is of the order of the structural symmetry deformation¹⁹. Indeed, calculating the electronic band structure using the (high-symmetric) macroscopically averaged *crystal structure* encoded in a minimal unit cell is not equivalent to calculating the (self-) *averaged band structures* in a large polymorphous cell having different local structural environments.

In the DFT calculations, to permit freedom of symmetry breaking, we deviate from the tradition of using the

minimal possible unit cell (which will unnecessarily restrict the symmetry of the displacements) and allow instead supercell replicas of the minimal cells. The input to the DFT is thus a $N_1 \times N_2 \times N_3$ replica, with periodic boundary conditions of a given macroscopic cell shape. The supercell size is systematically increased until the relaxed total energy per atom of a fixed cell shape saturates. For example, for tetragonal FeSe we use a 384-formula-unit cell (768 atoms per cell), although smaller supercells (96 formula unit) indicate that these effects have largely converged already by this point. To conserve the global unit cell symmetry, we restrict the supercell shape to the crystal system of the average crystal structure, which in the case of FeSe may be that either orthorhombic or tetragonal, depending on temperature. Subject to this constraint we give to each atom a random initial displacement off the high-symmetry position, then allow all cell internal atomic positions to relax, following quantum mechanically calculated forces to the minimal total energy structure. The total energy minimization calculations are done for several different spin order patterns (see supplementary S1) such as AFM1 (stripe antiferromagnetic), AFM2 (bi-stripe), AFM-checkerboard, FM (ferromagnetic), NM (non-magnetic with each atom having zero moment) and PM (paramagnetic, with vanishing total moment but arbitrary local moments obtained in energy minimization), to compare the total energies and relaxed structures of these different situations. Remarkably in these cases^{19,29,30}, the larger unit cells have lower total energy per formula unit than the monomorphous cells, suggesting that it can be an inherent property of some systems that should have a large unit cell. The structure obtained after the minimization is then used to compute the PDF for comparison with PDF measurements.

To interrogate possible electronic degeneracy removal, we use the variational supercell geometry in the band structure calculation. This, however, tends to produce complex E versus \mathbf{k} dispersion relations, making the analysis of band structure and comparison with ARPES cumbersome. A solution that retains the polymorphous nature of the system but reinstates the E versus \mathbf{k} relation in the base Brillouin zone is to unfold the supercell bands, which yields an “effective band structure”^{26–28} (EBS), providing a three-dimensional picture of the distribution of spectral density in the expanded Brillouin zone of the small monomorphous (crystallographic) unit cell.

Global versus local symmetries in FeSe

Iron selenide has an Fe-Se-Fe layered structure which is orthorhombic (space group *Cmme*) below 90 K³¹ and paramagnetic down to 0.4 K³², and transforms to a tetragonal structure (space group *P4/nmm*) above 90 K³³. The electronic structure of FeSe is interesting, among others, because of the apparent conflict between the

global symmetries implied by its X-ray diffraction structure versus the ones deduced from the electronic properties. In the low temperature orthorhombic phase, the symmetry gleaned from the observed Fermi surface⁵⁻⁷ corresponds to two twinned C_2 -symmetric bands, instead of the single C_2 symmetry mandated by the global space group symmetry measured in XRD. This nematicity of the low-T phase has been studied extensively, however there is still a divergence of opinions on its origins, be that orbital-selective correlation^{5,6}, or spin fluctuation^{8,9}.

Recent work focused on the *high temperature* tetragonal phase having nominal C_4 rotational symmetry^{11-13,34}. Applying local structure probe such as PDF by Frandsen et al.¹³, Konstantinova et al.¹¹ and by Koch et al.¹² showed that fitting the results in a phenomenological model required assuming symmetry-breaking local modes such as local orthorhombicity. However, in this approach a good fit to the measured PDF does not emerge from a physical principle (such as total energy minimum) but rather from brute force parametric fits. Furthermore, because there is no real space small periodic structure that is locally orthorhombic and globally tetragonal, the result of such a fit cannot be used as input to band theory to determine the ensuing electronic properties.

Structure, PDF and spin configuration from minimization of total internal energy

Our DFT calculation for (a) monomorphous and (b) polymorphous structures, each coupled to a specific spin configuration (shown in Figure S1) are summarized in Table I. The most stable configuration is the polymorphous structure in combination with AFM1 spin order, while the monomorphous cell with AFM1, AFM2 spin order and AFM-checkerboard are metastable. The non-magnetic phase with all atoms having zero spin (that has been used in many previous DFT studies²³⁻²⁵) is high in energy to the point of being physically irrelevant. The internal energy (DFT total energy) for different magnetic orders shown in Table I is consistent with previous suggestions^{35,36} that the tetragonal phase is fluctuated AFM1, or a mixture of AFM1 and AFM-CB. We find that the DFT total internal energy (no entropy) of the paramagnetic spin arrangement is only +32 meV/f.u. higher than the AFM1 spin arrangement (the lowest energy phase), indicating that such a paramagnetic phase should have a significant presence in the room-temperature FeSe compound.

The predicted atomic coordinates and lattice vectors are used to calculate the PDF (see details in Method section). The comparison between the calculated PDF and experiment PDF is shown in Figure 1. We find that all the monomorphous models give a poor agreement to the experimental PDF (see supplementary information section S2), *e.g.*, the misfit around 4 \AA^{12} as shown in Figure 1a, underscoring the experimental observation¹² that

the tetragonal phase is not described by a simple repeated structural motif. Furthermore, the hypothetical phenomenological orthorhombic model¹² ('monomorphous orthorhombic' model in Table I) that was used in the PDF studies to explain the short-range PDF data, gives a better fit than monomorphous tetragonal models in the short range but with serious misfits over long ranges ($r > 5 \text{ \AA}$)¹². Moreover, when combined with the lowest energy spin structure (AFM1), the phenomenological orthorhombic model has a rather high total energy of +414 meV/f.u. and is hence expected to be very unstable (Table I). Interestingly, the best agreement to the PDF data, which self-consistently provides a good fit over all length-scales, something the phenomenological modeling of the PDF was not able to do¹², is from the polymorphous description in combination with the AFM1 spin model (Table I), which we also find to be the lowest energy state. The overall weighted R-value (difference between observed $g_{\text{obs}}(r)$ and calculated $g_{\text{calc}}(r)$, see Methods section for details) is $R_w=0.071$ in the short range and $R_w=0.10$ in the long range, a good overall agreement given that all atomic positions are given by DFT total energy minimization with no fitting.

In Figure 2 we show the bond length distribution of all atom-atom pairs in the DFT determined monomorphous and polymorphous models. The PDF peak around 4 Å (the misfit peak for monomorphous tetragonal AFM1 model as shown in Figure 1a) comes from the shortest Se-Se distances. This set of Se-Se distances has three components that are close enough in length hence cannot be resolved in the PDF: in-plane (coplanar) Se-Se, intra-layer (non-coplanar) Se-Se, and inter-layer Se-Se. The first two distances separate Se ions that are part of the covalently bonded FeSe layer and the third is an Se-Se distance across the van der Waals coupled inter-layer spacing. That the polymorphous tetragonal model gives a better agreement for this ~4 Å peak than do monomorphous tetragonal models indicates that for both in-plane and inter-layer Se-Se environments, tetragonal FeSe has a distribution of symmetry-breaking distortions, *i.e.* it is in a polymorphous nature.

Identification of the local structural motifs

The minimization of the internal energy for a tetragonal supercell produces a complex set of atomic coordinates that, while they are readily used to compute the PDF profile, do not provide a simple picture of the local structural motifs present in the crystal. To gain more insight we identify two structural quantities from the total-energy-optimized supercells and compute them for each type of magnetic order (Figure 3): (a) The local distance along (001) direction between the center Fe plane and the Se plane, denoted as z_{se} (note that the averaged z_{se} measured from X-ray experiments at 300 K is 1.473 Å³⁷ and that all nearest Se-Se distances would be

equal when $z_{se}=1.381 \text{ \AA}$ which is the equal-distance condition); (b) The *local* cell orthorhombicity, η , defined as $\eta=2|a-b|/(a+b)$ where a and b are the lattice constants along x and y axis, while ‘local’ means η is defined to be r -dependent, *i.e.* $\eta(r)$. $\eta(r)$ can be extracted from the experimental PDF using PDF fits carried out over fixed r -ranges³⁸, or calculated from the supercell DFT models by doing statistical averages over all formula units over the same range r (see schematic plot in Figure 3b-c).

In our best total-energy-optimized supercell (AFM1 magnetic), z_{se} yields a distribution over the range 1.42-1.52 \AA as shown in Figure 3d (see Figure S2 for z_{se} distributions from all other magnetic order supercells). The comparison of $\eta(r)$ obtained from the tetragonal supercells, and from the experimental PDF¹², is shown in Figure 3e. The agreement is excellent, with both $\eta(r)$ showing 1.6-1.75% orthorhombic distortions in the local structure. The amplitude of the local orthorhombicity is much larger than the value from the average structure, where X-ray Bragg diffraction gives 0% for 90 K and above, 0.12% for 84 K and 0.4% for 40 K. This shows that, from polymorphous DFT energy minimizations, the local relaxations away from the monomorphous tetragonal structure actually result in correlated local displacements that are locally nematic with a much larger local nematicity than seen on average, in agreement with the observations from PDF.

Electronic degeneracy lifting caused by structural motifs

We now turn to consider the effect on the electronic structure of the various structural distortions we have discussed. First, we consider the effect of *global distortions*, *i.e.* uniformed z_{se} and r -independent η (monomorphous cases). We change the values of the two parameters, η and z_{se} , continuously in the ranges $0 < \eta < 2.5\%$ and $1.39 \text{ \AA} < z_{se} < 1.57 \text{ \AA}$. Figure 4a shows the DFT (GGA) non-magnetic band structure along Γ -M of the monomorphous tetragonal structure for reference. Note that this is the ‘DFT reference’ in many previous works^{23–25}. Following symbols used in previous studies, we mark the bands using different colors and small Greek letters corresponded to their orbital projections (red α for Fe $3d_{xz}$, blue β for Fe $3d_{yz}$, and green γ for Fe $3d_{xy}$). We find that:

(a) *Splitting between α and β ($\Delta_{\alpha\beta}$) is induced by orthorhombicity η . With $\eta = 0$ and no SOC, the α and β states are degenerate at Γ and M, but with $\eta > 0$ the degeneracy of α and β is broken, as observed in experiment^{5–7}. Such lift of degeneracy between α and β due to η also agrees with previous theoretical analysis as shown in reference³⁹ and¹². To achieve the experimentally observed $\Delta_{\alpha\beta}$ splitting in tetragonal phase (ARPES shows 20 meV on Γ and 60 meV on M^{6,9,40}), one needs $\eta=1.8$ -2%, which seems to be forbidden*

because the *averaged* orthorhombicity observed by X-ray Bragg diffraction is zero; however, by the polymorphous supercell, a *local* orthorhombicity as large as 1.75% is allowed even when the averaged orthorhombicity is constrained to zero (Figure 3e). Such relationship between η and $\Delta_{\alpha\beta}$ also indicates the polymorphous nature in FeSe.

(b) *The z_{Se} distance along (001) between Se and Fe layers does not break the degeneracy between α and β .* Instead, as z_{Se} increases the splitting between α/β and γ at Γ point is reduced, while the splitting between α/β and γ at the M point increases. The order between α/β and γ at Γ is reversed when $z_{\text{Se}} > 1.55 \text{ \AA}$. It agrees with previous theoretical studies³⁹. Note that in ARPES, for tetragonal phase the splitting between β and γ at Γ is reported as 40 meV^{6,9,40}, which, according to this monomorphous model, corresponds to $z_{\text{Se}} = 1.52 \text{ \AA}$, however does not agree with the value of 1.473 \AA as measured by X-ray diffraction³⁷. In other words, monomorphous model fails to achieve the agreement with both ARPES and X-ray measurement.

Band unfolding and comparison with ARPES

To compare the band-structures of the polymorphous DFT calculations, it is necessary to unfold the bands into the fundamental unit cell in which the experimental ARPES bands are analyzed. The approach we take here is to use an “Effective Band Structure” (EBS) method^{26–28}. Similar to ARPES, the EBS method provides a three-dimensional picture of the spectral function with E- and k-dependent features including coherent (dispersive term, or ‘sharpness’) and incoherent (band nondispersive broadening, or ‘fuzziness’) spectral weights that can be directly compared to ARPES data. All the coherent and incoherent features are naturally produced by the polymorphous nature of the many local environments in the compound. See Methods section for details.

The comparison between experimental ARPES^{6,9,40} and calculated *monomorphous* (GGA+U, non-magnetic, tetragonal, 1 formula unit per cell) band structure, and between ARPES and unfolded *polymorphous* (GGA+U, paramagnetic, tetragonal, 384 formula unit per cell) band structure is shown in Figure 5. The ARPES results are extracted from Ref ^{6,9,40} and shown as black hollow circles (identical in Figure 5a and 5b); the monomorphous band structure is shown in Figure 5a as blue lines, and it is the same one as shown in Figure 4a; the polymorphous unfolded band structure, or EBS, is shown in Figure 5b by 2D contours.

In each of the three results (ARPES, monomorphous model, polymorphous model) there are three bands appearing in the energy range nearby Fermi level; we mark them as α , β , and γ , which are consistent with Figure 4 (and previous studies). As shown in Figure 5a, the monomorphous model fails to obtain good electronic

band structure if compared with ARPES observations: Neither the energies of α - γ states at Γ , nor the dispersions (*i.e.* effective mass) of those states nearby Γ agree with experimental results. Such failure of the monomorphous model is often attributed to some intrinsic failure of the electronic interactions encoded in DFT. However, Figure 5b shows that if we allow electronic system to couple with the polymorphous network without the restriction of small cell, and then unfold the results back to the primitive BZ we can achieve a good agreement between DFT and ARPES results. The calculated EBS not only reproduces the correct band order and band splitting among α - γ at Γ , but also provides the correct effective mass for each of the three bands.

Implications and prospects

The main finding of this study is that significant anomalies in the atomic and electronic structures of the canonical iron-based superconductor, FeSe, emerge from the existence of an intrinsic (non-thermal) distribution of local positional with spin motifs mandated by the chemical bonding at low T. As such, this polymorphous nature can be rather straightforwardly reproduced from DFT calculations without the need to invoke strong electron correlation effects, but only if the DFT is allowed to relax an enlarged supercell. By removing the constraint of a small crystallographic unit cell, the DFT can find more stable atomic arrangements that self-consistently explain both observations of enhanced nematicity in the local structure and a tetragonal or weakly orthorhombic long-range structure. The locally relaxed structures break the degeneracy of the Fe orbitals and explain the electronic nematicity in these materials. The implication of this discovery is that band structures of such compounds cannot be performed with the traditional, minimally sized unit cell obtained from the macroscopically averaged structure gleaned from X-ray diffraction. This realization holds the potential of crossing sub discipline divides and affecting other areas of materials physics and chemistry where polymorphous networks are likely to abound. Future prospects include the challenge of sorting out theoretically and experimentally polymorphous networks that have high global symmetry with low (broken) local symmetry from the traditional monomorphous networks where repeated single (or very few) motifs suffice to describe the structure on all length scales. Electronic anomalies observed already in monomorphous structures could reflect strong dynamic correlations, whereas anomalies observed in symmetry-broken polymorphous networks could represent primarily structurally- induced anomalies.

Methods

DFT calculation. All calculations are done using VASP with PAW-PBE pseudopotentials and GGA+U (U=0.875 V on Fe 3d). The cutoff energy is 350 eV. Van der Waals interaction has been involved in all calculations using opt86b method. We don't consider the spin-orbit coupling (SOC) in our calculations. The size of each model (all monomorphous small cells and polymorphous supercells) has been shown in Table I. To make the total energies between different cells comparable, we use an equivalent k-point mesh for total energy calculations in all cells. Magnetic orderings are shown in Figure S1. Paramagnetic supercell is generated following the special quasirandom structure (SQS) method using ATAT code, the same procedure as applied in ref¹⁷. All monomorphous cells are fully optimized (all lattice vectors as well as internal atomic positions are fully optimized) by DFT total energy minimization before we calculate the total energies and band structures; all polymorphous cells are constrained to have the same lattice vectors as the AFM1 monomorphous cell, and then fully optimized internally (only internal atomic positions are optimized).

PDF from DFT. All calculations for PDF from DFT-optimized structure are done using PDFgui software⁴¹. For tetragonal FeSe, Q_{damp} and Q_{broad} are set to 0.042 and 0.01, while s_{ratio} and r_{cut} are set to 1.0 and 0, respectively, the same values as used in ref¹²; scaling factor, δ_1 and atomic displacement parameters (ADPs) are fitted by PDFgui (values listed in supplementary information Table S1). For the 'monomorphous orthorhombic' model in Table 1, the lattice constants and atomic positions are directly taken from ref.12; for all other models, all atomic positions and lattice constants are given by DFT total energy optimization without fitting or postprocessing.

The overall weighted R-value. We use a weighted agreement factor R_w to assess the agreement between calculated and observed PDF, which is given by

$$R_w = \sqrt{\frac{\sum_{i=1}^n [g_{\text{obs}}(r_i) - g_{\text{calc}}(r_i, P)]^2}{\sum_{i=1}^n [g_{\text{obs}}(r_i)]^2}}, \quad (1)$$

Effective band structure: basic concept. The basic concept of EBS can be described using the following equations. Assume in supercell $|Km\rangle$ is the m-th electronic eigen state at K in supercell BZ whereas in primitive cell $|k;n\rangle$ is the n-th eigen state at k_i in primitive BZ, then each $|Km\rangle$ can be expanded on a complete set of $|k;n\rangle$ where $K = k_i - G_i$, and G_i being reciprocal lattice vectors in the supercell BZ, which is the folding mechanism²⁸

$$|Km\rangle = \sum_{i=1}^{N_K} \sum_n F(k_i, n; K, m) |k_i n\rangle, \quad (2)$$

The supercell band structure at K can then be *unfolded* back to k_i by calculating the spectral weight $P_{Km}(k_i)$

$$P_{Km}(k_i) = \sum_n |\langle Km | k_i n \rangle|^2 \quad (3)$$

$P_{Km}(k_i)$ represents ‘how much’ Bloch characteristics of wavevector k_i has been preserved in $|Km\rangle$ when $E_n = E_m$. The EBS is then calculated by spectral function $A(k_i, E)$

$$A(k_i, E) = \sum_m P_{Km}(k_i) \delta(E_m - E) \quad (4)$$

Acknowledgements

We would like to thank Emil Bozin and Robert Koch for insightful discussions, help with PDF computations, and for sharing their data from their publication (ref¹²). The work in the Zunger group and Billinge group was supported by the US National Science Foundation through grant DMREF-1921949. The calculations were done using the Extreme Science and Engineering Discovery Environment (XSEDE), which is supported by the National Science Foundation grant number ACI-1548562.

Author contributions

A.Z conceived the concept and devised the analysis. Z.W performed the DFT calculations and contributed to the theoretical analysis and discussion. X.Z contributed to the theoretical discussion of the polymorphous network. S.J.L.B contributed to the experimental PDF data (Ref 12), and the analysis and discussion of the experimental results. Z.W wrote the paper with contributions from all authors.

Competing interests

The authors declare no competing interests.

References

1. Goldschmidt, V. M. Die Gesetze der Krystallochemie. *Naturwissenschaften* **14**, 477–485 (1926).
2. Pauling, L. *The Nature of the Chemical Bond...* vol. 260.
3. Peierls, R. E. *Quantum theory of solids*. (Clarendon Press, 1996).
4. Jahn, H. A. & Teller, E. Stability of polyatomic molecules in degenerate electronic states—I—Orbital degeneracy. *Proc. R. Soc. Lond. Ser. -Math. Phys. Sci.* **161**, 220–235 (1937).
5. Shimojima, T. *et al.* Lifting of xz/yz orbital degeneracy at the structural transition in detwinned FeSe. *Phys. Rev. B* **90**, 121111 (2014).
6. Watson, M. D. *et al.* Emergence of the nematic electronic state in FeSe. *Phys. Rev. B* **91**, 155106 (2015).
7. Watson, M. D., Haghighirad, A. A., Rhodes, L. C., Hoesch, M. & Kim, T. K. Electronic anisotropies revealed by detwinned angle-resolved photo-emission spectroscopy measurements of FeSe. *New J. Phys.* **19**, 103021 (2017).
8. Yin, Z. P., Haule, K. & Kotliar, G. Kinetic frustration and the nature of the magnetic and paramagnetic states in iron pnictides and iron chalcogenides. *Nat. Mater.* **10**, 932–935 (2011).
9. Yi, M., Zhang, Y., Shen, Z.-X. & Lu, D. Role of the orbital degree of freedom in iron-based superconductors. *Npj Quantum Mater.* **2**, 1–12 (2017).
10. Egami, T. & Billinge, S. J. *Underneath the Bragg peaks: structural analysis of complex materials - 2nd*

Edition. (Elsevier, 2012).

11. Konstantinova, T. *et al.* Photoinduced dynamics of nematic order parameter in FeSe. *Phys. Rev. B* **99**, 180102 (2019).
12. Koch, R. J. *et al.* Room temperature local nematicity in FeSe superconductor. *Phys. Rev. B* **100**, 020501 (2019).
13. Frandsen, B. A., Wang, Q., Wu, S., Zhao, J. & Birgeneau, R. J. Quantitative characterization of short-range orthorhombic fluctuations in FeSe through pair distribution function analysis. *Phys. Rev. B* **100**, 020504 (2019).
14. Born, M. & Huang, K. *Dynamical theory of crystal lattices*. (Clarendon press, 1954).
15. Kent, P. R. C. & Zunger, A. Theory of electronic structure evolution in GaAsN and GaPN alloys. *Phys. Rev. B* **64**, 115208 (2001).
16. Wang, Z., Luo, J.-W. & Zunger, A. Alloy theory with atomic resolution for Rashba or topological systems. *Phys. Rev. Mater.* **3**, 044605 (2019).
17. Trimarchi, G., Wang, Z. & Zunger, A. Polymorphous band structure model of gapping in the antiferromagnetic and paramagnetic phases of the Mott insulators MnO, FeO, CoO, and NiO. *Phys. Rev. B* **97**, 035107 (2018).
18. Varignon, J., Bibes, M. & Zunger, A. Origin of band gaps in 3d perovskite oxides. *Nat. Commun.* **10**,

1658 (2019).

19. Zhao, X., Dalpian, G. M., Wang, Z. & Zunger, A. The polymorphous nature of cubic halide perovskites. *ArXiv190509141 Cond-Mat* (2019).
20. Torrance, J. B., Lacorre, P., Nazzari, A. I., Ansaldo, E. J. & Niedermayer, Ch. Systematic study of insulator-metal transitions in perovskites $RNiO_3$ ($R=Pr,Nd,Sm,Eu$) due to closing of charge-transfer gap. *Phys. Rev. B* **45**, 8209–8212 (1992).
21. Reaney, I. M., Colla, E. L. & Setter, N. Dielectric and Structural Characteristics of Ba- and Sr-based Complex Perovskites as a Function of Tolerance Factor. *Jpn. J. Appl. Phys.* **33**, 3984 (1994).
22. Glazer, A. M. The classification of tilted octahedra in perovskites. *Acta Crystallogr. B* **28**, 3384–3392 (1972).
23. Borisenko, S. V. *et al.* Direct observation of spin-orbit coupling in iron-based superconductors. *Nat. Phys.* **12**, 311–317 (2016).
24. Tamai, A. *et al.* Strong Electron Correlations in the Normal State of the Iron-Based $FeSe_{0.42}Te_{0.58}$ Superconductor Observed by Angle-Resolved Photoemission Spectroscopy. *Phys. Rev. Lett.* **104**, 097002 (2010).
25. Gerber, S. *et al.* Femtosecond electron-phonon lock-in by photoemission and x-ray free-electron laser. *Science* **357**, 71–75 (2017).

26. Wang, L.-W., Bellaiche, L., Wei, S.-H. & Zunger, A. "Majority Representation" of Alloy Electronic States. *Phys. Rev. Lett.* **80**, 4725 (1998).
27. Popescu, V. & Zunger, A. Effective band structure of random alloys. *Phys. Rev. Lett.* **104**, 236403 (2010).
28. Popescu, V. & Zunger, A. Extracting E versus $k \rightarrow$ effective band structure from supercell calculations on alloys and impurities. *Phys. Rev. B* **85**, 085201 (2012).
29. Hart, G. L. W. & Zunger, A. Origins of Nonstoichiometry and Vacancy Ordering in $\text{Sc}_{1-x}\square_x\text{S}$. *Phys. Rev. Lett.* **87**, 275508 (2001).
30. Barabash, S. V., Blum, V., Müller, S. & Zunger, A. Prediction of unusual stable ordered structures of Au-Pd alloys via a first-principles cluster expansion. *Phys. Rev. B* **74**, 035108 (2006).
31. Margadonna, S. *et al.* Crystal structure of the new FeSe_{1-x} superconductor. *Chem. Commun.* 5607–5609 (2008) doi:10.1039/B813076K.
32. Song, C.-L. *et al.* Direct Observation of Nodes and Twofold Symmetry in FeSe Superconductor. *Science* **332**, 1410–1413 (2011).
33. Hsu, F.-C. *et al.* Superconductivity in the PbO-type structure α -FeSe. *Proc. Natl. Acad. Sci.* **105**, 14262–14264 (2008).
34. Wen, Y.-C. *et al.* Gap Opening and Orbital Modification of Superconducting FeSe above the Structural Distortion. *Phys. Rev. Lett.* **108**, 267002 (2012).

35. Glasbrenner, J. K. *et al.* Effect of magnetic frustration on nematicity and superconductivity in iron chalcogenides. *Nat. Phys.* **11**, 953–958 (2015).
36. Wang, Q. *et al.* Magnetic ground state of FeSe. *Nat. Commun.* **7**, 1–7 (2016).
37. Phelan, D. *et al.* Neutron scattering measurements of the phonon density of states of FeSe_{1-x} superconductors. *Phys. Rev. B* **79**, 014519 (2009).
38. Qiu, X., Proffen, Th., Mitchell, J. F. & Billinge, S. J. L. Orbital Correlations in the Pseudocubic O and Rhombohedral R Phases of LaMnO₃. *Phys. Rev. Lett.* **94**, 177203 (2005).
39. Andersen, O. K. & Boeri, L. On the multi-orbital band structure and itinerant magnetism of iron-based superconductors. *Ann. Phys.* **523**, 8–50 (2011).
40. Kushnirenko, Y. S. *et al.* Anomalous temperature evolution of the electronic structure of FeSe. *Phys. Rev. B* **96**, 100504 (2017).
41. Farrow, C. L. *et al.* PDFfit2 and PDFgui: computer programs for studying nanostructure in crystals. *J. Phys. Condens. Matter* **19**, 335219 (2007).

Table 1 | Parameters and properties of different FeSe models. Magnetic order: NM = nonmagnetic; FM = ferromagnetic; AFM = antiferromagnetic; AFM-CB = AFM-checkerboard; AFM1 = AFM-stripe; AFM2 = AFM-bistripe (see Figure S1 for details). Cell size is in number of formula units per cell. Crystallographic parameter z_{Se} is the distance in (001) direction between Se layer and center Fe layer, given also as the Wyckoff position of Se atom in fractional coordinate. DFT total energies are relative to reference (AFM1). R-factor comparing calculated to measured PDF is given by the weighted R-factor R_w (see Method section) in short range (1.5-5 Å) and long range (5-50 Å).

	Magnetic order	Cell size (f.u./cell)	a, b, c (Å)	z_{Se} (Å), Wyckoff	DFT total energy (meV/f.u.)	Short-range R_w^a	Long-range R_w^a
Experimental Tetragonal	-	-	5.334, 5.334, 5.524 ^b	1.473, 0.267 ^b	-	-	-
Monomorphous Tetragonal	NM	2	5.138, 5.138, 5.452 ^c	1.401, 0.257 ^c	+230	0.64	0.80
	FM	2	4.964, 4.964, 5.724 ^c	1.642, 0.287 ^c	+127	0.64	0.92
	AFM-CB	4	5.242, 5.242, 5.594 ^c	1.481, 0.265 ^c	+74	0.31	0.47
	AFM2	4	5.166, 5.166, 5.772 ^c	1.581, 0.274 ^c	+22	0.52	0.59
	AFM1 (ref)	4	5.338, 5.338, 5.521 ^c	1.473, 0.267 ^c	0	0.11	0.10
Polymorphous Tetragonal	AFM1	384	5.338, 5.338, 5.521 ^d	1.470, 0.266 ^e	-3.4	0.073	0.15
	PM	384	5.338, 5.338, 5.521 ^d	1.466, 0.266 ^e	+32	0.078	0.17
Monomorphous Orthorhombic	-	4	5.321, 5.412, 5.495 ^f	1.457, 0.265 ^f	+414	0.045	0.46

(a) Experimental PDF from ref¹²; (b) from ref³⁷; (c) from DFT optimization for tetragonal phase (lattice constants a and c are optimized; all internal atomic positions are optimized); (d) from DFT optimization for internal atomic positions (lattice vectors are constrained); (e) from statistical average after DFT optimization; (f) from ref¹²

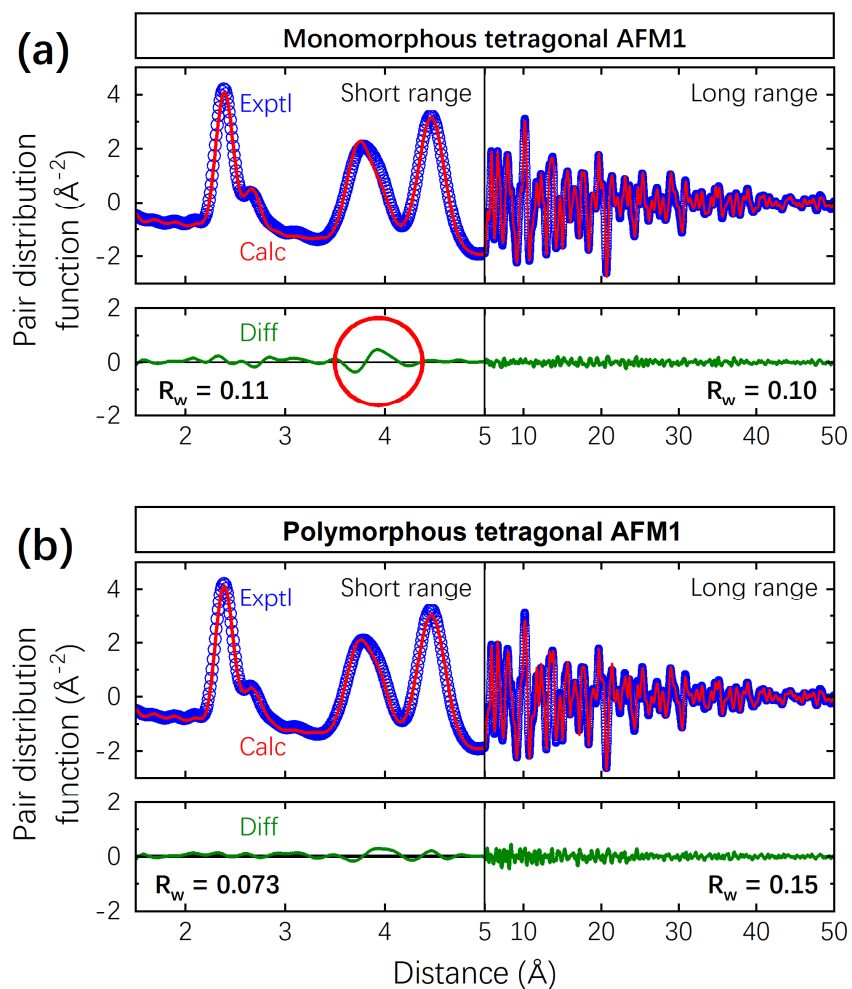


Figure 1 | The comparison between an experimentally measured PDF (blue dots) and calculated PDF (red lines), shown together with the difference (green lines) for (a) monomorphous tetragonal AFM1 phase (4 f.u./cell), and (b) polymorphous tetragonal AFM1 phase (384 f.u./cell). The overall R-factors are also given. Results for other monomorphous structures are given in supplementary section S2.

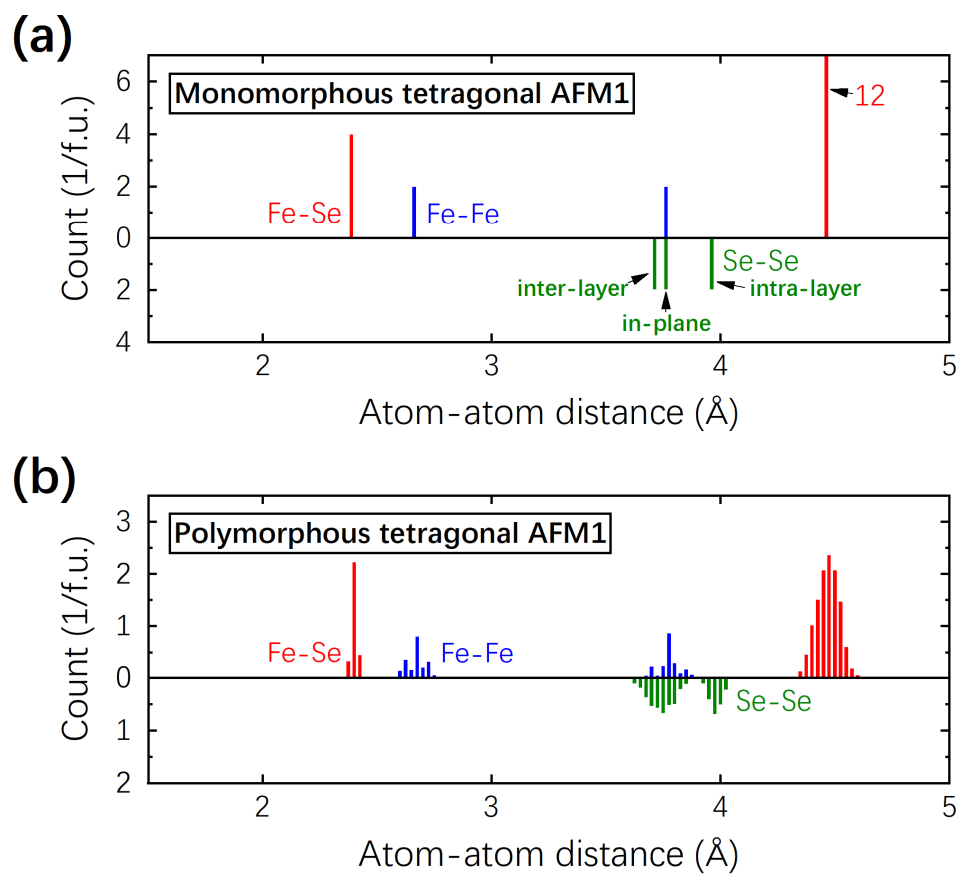


Figure 2 | Bond length distribution of all atom-atom pairs for (a) monomorphous tetragonal AFM1 phase and (b) polymorphous tetragonal AFM1 phase.

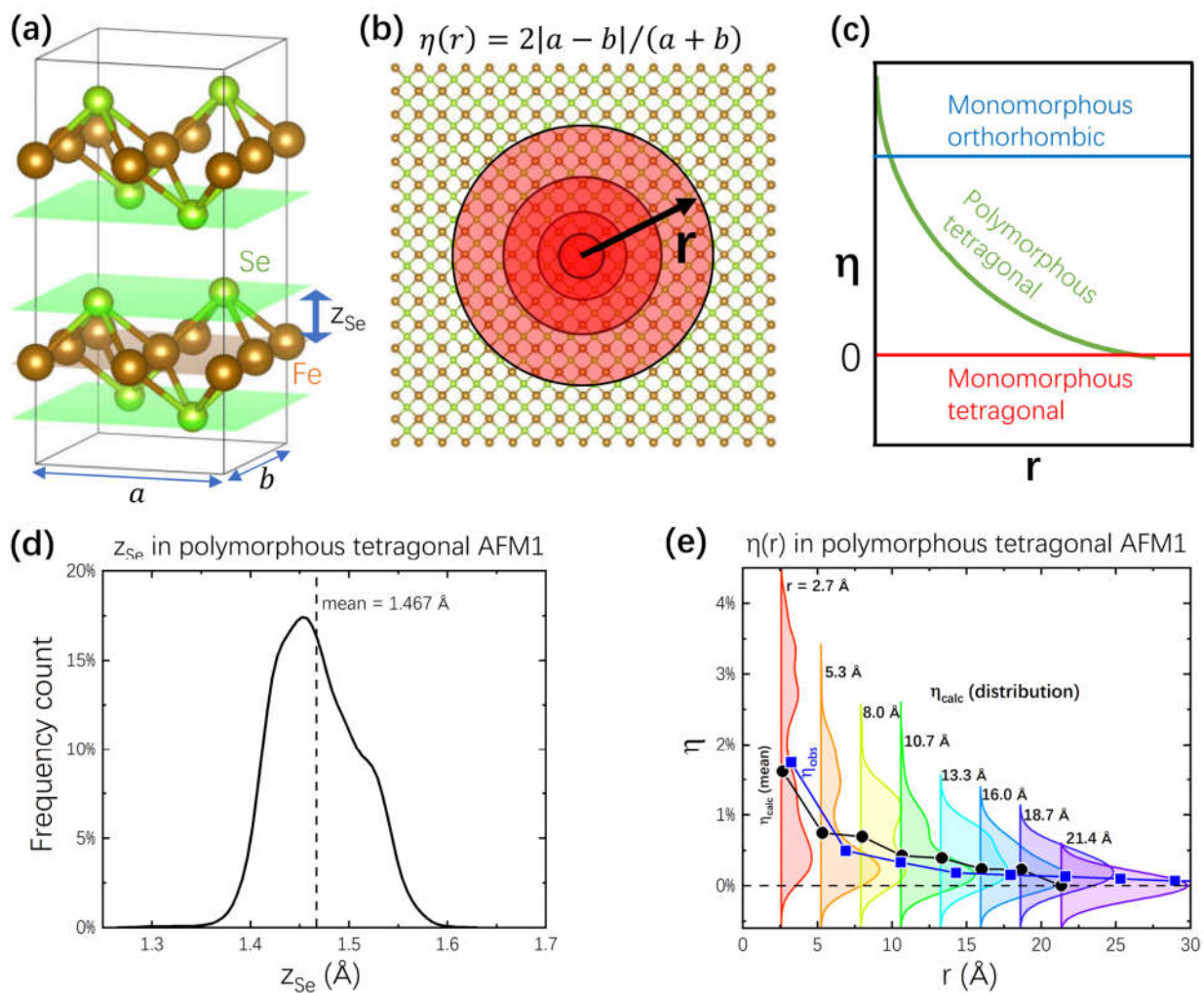


Figure 3 | The two structural displacements in FeSe, and the comparison between calculation and experiment. (a)-(c) Definition of the two structural displacements: (a) Atomic model of FeSe showing z_{Se} ; (b) schematic plot showing the r -dependent orthorhombicity $\eta(r)$; (c) schematic plot for $\eta(r)$ behavior in monomorphous orthorhombic cell (blue line), monomorphous tetragonal cell (red line), and polymorphous tetragonal supercell (green line). (d) and (e) Comparison between calculation and experiment: (d) The distribution (solid line) and mean value (dash line) of z_{Se} in polymorphous tetragonal AFM1 supercell (384 f.u./cell), note that the experimental value is 1.473 Å³⁷; (e) the distribution (colored areas) and the mean values (black dots with line) of $\eta_{\text{calc}}(r)$ in the same supercell, compared with the observed $\eta_{\text{obs}}(r)$ (blue squares with line) from 300 K X-ray experiment¹².

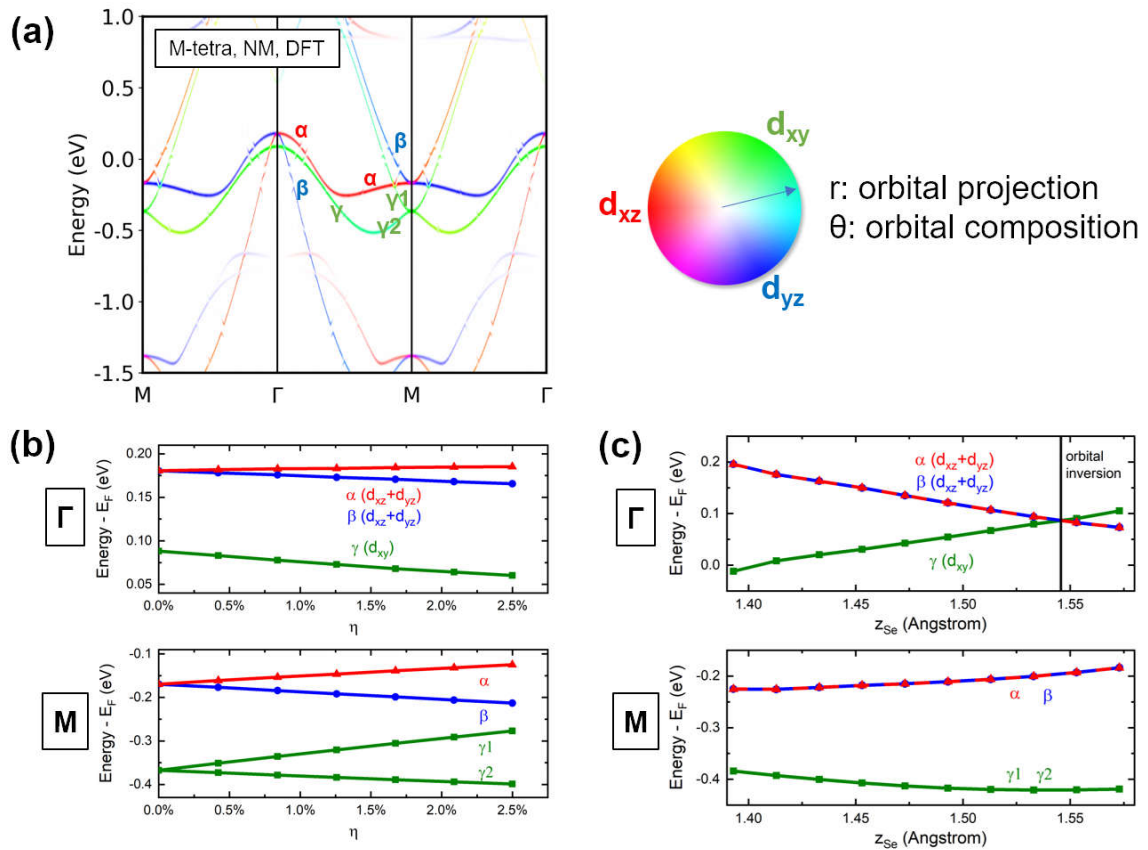


Figure 4 | The local displacement induced symmetry-breaking in the DFT electronic band structure in a monomorphous (M-), non-magnetic (NM), tetragonal (tetra.) cell. Red α for Fe 3d_{xz}, blue β for Fe 3d_{yz}, and green γ for Fe 3d_{xy}. (b) The lifting of degeneracy at the gamma and M points between α and β , and between $\gamma 1$ and $\gamma 2$, at different η . (c) The eigenvalue shifts of α/β degenerates, γ band, and $\gamma 1/\gamma 2$ degenerates, at different z_{Se} .

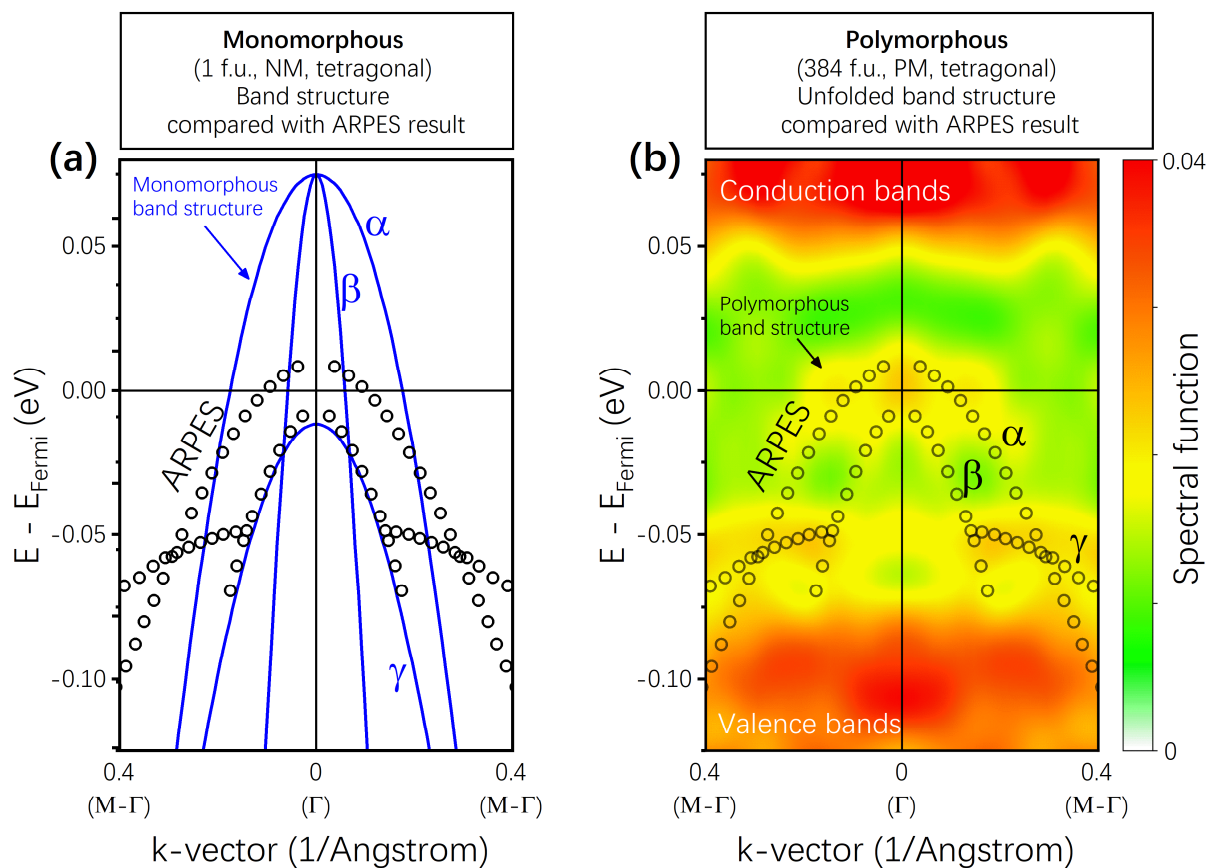


Figure 5 | Comparison of tetragonal FeSe electronic structure from DFT calculation and from ARPES measurement. The band structure in blue lines shown in (a) is from the conventional, 1 formula unit per cell, non-magnetic model (plotted along M- Γ -M in the primitive Brillouin zone), while the 2D color contour EBS shown in (b) is from the 384 formula unit, paramagnetic supercell (unfolded to the same primitive Brillouin zone as in (a)). ARPES results are shown by black hollow circles in both (a) and (b). The three bands nearby Fermi level are marked as α , β , and γ , the same small Greek letters as used in Figure 4.